AIP | Journal of Applied Physics

Ergodicity reflected in macroscopic and microscopic field-dependent behavior of BNT-based relaxors

Robert Dittmer, Danka Gobeljic, Wook Jo, Vladimir V. Shvartsman, Doru C. Lupascu, Jacob L. Jones, and Jürgen Rödel

Citation: Journal of Applied Physics **115**, 084111 (2014); doi: 10.1063/1.4867157
View online: http://dx.doi.org/10.1063/1.4867157
View Table of Contents: http://scitation.aip.org/content/aip/journal/jap/115/8?ver=pdfcov
Published by the AIP Publishing

Ergodicity reflected in macroscopic and microscopic field-dependent behavior of BNT-based relaxors

Robert Dittmer,[1] Danka Gobeljic,[2] Wook Jo,[1,a)] Vladimir V. Shvartsman,[2] Doru C. Lupascu,[2] Jacob L. Jones,[3,4] and Jürgen Rödel[1]
[1]*Institute of Materials Science, Technische Universität Darmstadt, Petersenstraße 23, 64287 Darmstadt, Germany*
[2]*Institute for Material Science and Center for Nanointegration Duisburg-Essen (CeNIDE), University of Duisburg-Essen, Universitätsstraße 15, 45141 Essen, Germany*
[3]*Department of Materials Science and Engineering, University of Florida, Gainesville, Florida 32611-6400, USA*
[4]*Department of Materials Science and Engineering, North Carolina State University, Raleigh, North Carolina 27695, USA*

(Received 9 December 2013; accepted 17 February 2014; published online 27 February 2014)

The effect of heterovalent B-site doping on ergodicity of relaxor ferroelectrics is studied using $(1-y)(0.81Bi_{1/2}Na_{1/2}TiO_3\text{-}0.19Bi_{1/2}K_{1/2}TiO_3)\text{-}yBiZn_{1/2}Ti_{1/2}O_3$ (BNT-BKT-BZT) with $y = \{0.02;0.03;0.04\}$ as a model system. Both the large- and small-signal parameters are studied as a function of electric field. The crystal structure is assessed by means of neutron diffraction in the initial state and after exposure to a high electric field. In order to measure ferroelastic domain textures, diffraction patterns of the poled samples are collected as a function of sample rotation angle. Piezoresponse force microscopy (PFM) is employed to probe the microstructure for polar regions at a nanoscopic scale. For low electric fields $E < 2\,kV{\cdot}mm^{-1}$, large- and small-signal constitutive behavior do not change with composition. At high electric fields, however, drastic differences are observed due to a field-induced phase transition into a long-range ordered state. It is hypothesized that increasing BZT content decreases the degree of non-ergodicity; thus, the formation of long-range order is impeded. It is suggested that frozen and dynamic polar nano regions exist to a different degree, depending on the BZT content. This image is supported by PFM measurements. Moreover, PFM measurements suggest that the relaxation mechanism after removal of the bias field is influenced by surface charges. © *2014 AIP Publishing LLC*.
[http://dx.doi.org/10.1063/1.4867157]

I. INTRODUCTION

Against the background of increasing environmental awareness, the distribution of lead-containing devices throughout consumer products faces increasing restrictions.[1,2] This development triggered extensive research efforts to find lead-free alternatives to lead zirconate titanate $PbZr_xTi_{1-x}O_3$ (PZT).[3,4] Despite several promising findings in recent years, it has become evident that one single compound will not likely replace lead-containing materials across the whole diverse range of piezoelectric applications. Rather, multiple, tailored lead-free solutions are sought for individual applications. In the case of actuator applications, where large displacements are always preferred, pseudo-binary and -ternary solid solutions based on $Bi_{1/2}Na_{1/2}TiO_3$ (BNT) were reported to provide outstanding electromechanical performance—partially competing with or even surpassing PZT.[5–8] Moreover, it was demonstrated that these large strains are, in general, associated with large forces.[9]

This class of materials is appealing not just from an application point of view but also from a scientific perspective. The peculiar field-dependent behavior and the underlying physical mechanism for the observed large strain have long been disputed. Diffraction studies[10–14] and piezoresponse force microscopy (PFM) measurements[15] suggested that a reversible field-induced phase transition should take place, resulting in the creation and the collapse of long-range order during cycling. Consequently, a lack of remanence enables large strains during every cycle.[16]

The pseudobinary solid solution $0.8Bi_{1/2}Na_{1/2}TiO_3\text{-}0.2Bi_{1/2}K_{1/2}TiO_3$ (80BNT-20BKT) displays a high remanent polarization of $0.384\,C{\cdot}m^{-2}$ and accordingly good piezoelectric properties with $d_{33} = 157\,pm{\cdot}V^{-1}$.[17,18] The unbiased structure determined via XRD is pseudocubic with narrow reflections and virtually no non-cubic distortions.[19] For 80BNT-20BKT modified with 4 mol. % BZT, a large strain was found. It was suggested that this class of BNT-based materials is relaxor ferroelectric undergoing a field-induced phase transition from the relaxor state to a long-range ordered state.[20] This means that the initially nanoscopically small polar regions (polar nano-regions, PNRs) are triggered to grow into micron-sized domains with the application of electric field. Depending on the concentration of heterovalent ions in the perovskite lattice, the order/disorder state is altered. Due to the enhancement of random electric fields[21] with the concentration of foreign ions, an initially non-ergodic system renders ergodic

a)Author to whom correspondence should be addressed. Electronic mail: jo@ceramics.tu-darmstadt.de. Telephone: +49 6151 16-6302. Fax: +49 6151 16-6314.

at the same temperature; thus, the degree of non-ergodicity, referred to as *DoN* in the following, may decrease.

II. ERGODICITY WITHIN THE SCOPE OF THIS WORK

It seems appropriate to briefly recap the concept of ergodicity and non-ergodicity. The term "ergodic" was elaborated by Boltzmann from the Greek words for work (*ergon*) and path (*odos*) in order to describe energy surfaces in statistical mechanics.[22] A statistical process is referred to as ergodic when, under appropriate conditions, time average is equal to ensemble average. A persuasive example of ergodicity is encountered when dices are thrown as sketched in a simplified manner in Figure 1. The time average, which is the average of 6×10^6 subsequent throws of one dice, equals the ensemble average, which is the average of 6×10^6 dice each thrown once. This system becomes non-ergodic when the initial state of the 6×10^6 dice is not random anymore. This would be the case, for example, when two faces of the dice are magnetic so that all "twos" are attracted to "fives" but repelled by other "twos." In that case, the time average and the ensemble average would be different and ergodicity is broken.

In solid state physics, the concept of ergodicity and non-ergodicity was employed to describe magnetic spin glasses.[23] These structurally disordered systems exhibit a freezing transition at a temperature T_f. Above T_f, the system is magnetically disordered and ergodic; however, upon cooling through T_f the spins are frozen in. This means that ergodicity is broken since some relaxation times diverge and, consequently, the stable ground state cannot be reached at laboratory time scales.

Viehland *et al.*[24,25] proposed the terminology for relaxor ferroelectrics, which are likewise disordered systems with a freezing transition in analogy with the magnetic spin glasses. Below the Burns temperature T_B, polar entities of nanoscopic size, so called PNRs, appear within the metrically cubic matrix.[26] As the PNRs are highly dynamic and not correlated, the relaxor behaves in an ergodic manner. At T_f, the PNRs begin to freeze and to interact; thus, ergodicity is broken and the relaxor exhibits increasingly glass-like behavior. As the interactions are frustrated, a configuration with random polarization directions is obtained instead of a parallel alignment as in ferroelectrics. A ferroelectric state, however, can be induced from a non-ergodic relaxor by application of a sufficiently strong electric field.[27]

It is important to point out that the term "ergodic" is not used as strict for relaxors as it is in statistics, where a system is called ergodic only when time average and ensemble average lead to the same state with a probability of 100%. For relaxors, in contrast, it is more correct to speak about quasi-ergodicity or varying degrees of non-ergodicity.

In this work, we study the effect of a varying degree of non-ergodicity on the functional, structural, and microstructural properties and the interplay thereof in order to elucidate the peculiar field-dependent constitutive behavior of BNT-based lead-free piezoceramics. For this reason, the BZT content of the model system $(1 - y)$(0.81BNT-0.19BKT)-yBZT is systematically varied. It is demonstrated that the large-signal properties are virtually independent of BZT content at small electric fields, however, the electrical properties change dramatically beyond a composition-dependent threshold field. To investigate this change, neutron diffraction (ND) and PFM are utilized. Compared to X-ray diffraction, the sensitivity of neutron diffraction for oxygen ions is increased, allowing a detection of subtle changes of the oxygen-octahedral geometry. In addition, rotation-angle-resolved diffraction patterns allow the detection of domain textures. Moreover, the PFM technique affords not only the imaging of the microstructure but also the manipulation of

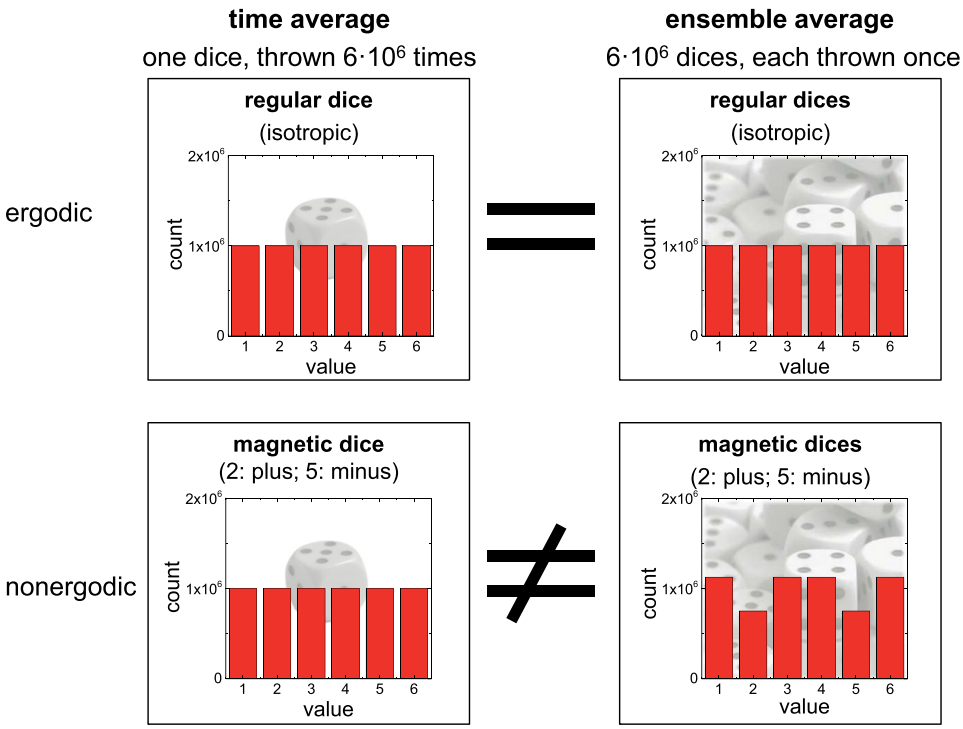

FIG. 1. A simple example for ergodicity and non-ergodicity.

polar regions at a nanoscopic scale by means of a tip bias field.

III. EXPERIMENTAL DESCRIPTION

A. Sample preparation

The investigated compositions within this work are $(1-y)(0.81Bi_{1/2}Na_{1/2}TiO_3\text{-}0.19Bi_{1/2}K_{1/2}TiO_3)\text{-}yBiZn_{1/2}Ti_{1/2}O_3$ with $y = 0.02$, 0.03, and 0.04, referred to as 2BZT, 3BZT, and 4BZT. Ceramic powders were made by means of a mixed oxide route with details of the processing given elsewhere.[28] The pressed samples were sintered for 3 h at 1100 °C. In order to minimize the evaporation of volatile elements, the samples were partially covered in a powder bed of the respective composition. By subsequent grinding, the desired sample geometry was adjusted.

For electrical measurements, disc-shaped samples with 7 mm in diameter and about 0.7 mm in height were electroded using silver paste (Gwent Electronic Materials Ltd, Pontypool, UK) and subsequent burn-in process at 400 °C. Preparation of specimens for PFM measurements included one-side surface polishing down to optical quality by subsequent use of polycrystalline diamond pastes (DP-Paste P by Struers A/S, Ballerup, Denmark) with abrasive particles of 15 μm, 9 μm, 3 μm, 1 μm, and $^1/_4$ μm. For neutron diffraction measurements, bar-type samples with the geometry of $3 \times 3 \times 30$ mm^3 were used. The electrodes were applied by sputter-coating gold on two opposing long faces.

B. Electrical measurements

For the measurement of the large-signal properties, the sample was submerged in silicone oil (AK35 or AK200, Wacker Chemie GmbH, München, Germany) bath to allow the application of electric fields up to 6 kV·mm^{-1}. Electric contact was established by a point contact on both sides of samples. A function generator (Agilent 33220 A, Agilent Technologies Deutschland GmbH, Böblingen, Germany) was used to supply a voltage source (20/20 C, TREK, Inc., Medina, NY, USA) with a triangular waveform at the frequency of 1 Hz. The amplitude of the high voltage signal was varied in steps of 1 kV·mm^{-1} from 1 kV·mm^{-1} to 6 kV·mm^{-1}. To assess the amplitude-dependent evolution of the remanent strain, samples were measured from the virgin state with intermediate annealing steps on a hot plate at 400 °C. Polarization changes were measured with a Sawyer-Tower setup, while strain s was measured simultaneously with an optical sensor (D63, Philtec, Inc., Annapolis, MD, USA).

The relative permittivity $\varepsilon_{r,33}$ and piezoelectric coefficient d_{33} were measured as a function of bias field by superimposing a small AC signal of 1 kHz and 5 V_{rms} to a large-signal waveform. The large signal was increased in steps of 100 V_{DC} for 5.5 s for each step yielding an efficient frequency of approximately 1 mHz. Using two lock-in amplifiers (SR830, Scientific Instruments, West Palm Beach, FL, USA), small changes in polarization and strain were detected allowing the measurement of d_{33} and $\varepsilon_{r,33}$. The setup is described in detail elsewhere.[29]

C. Neutron diffraction

The ND experiments were performed at the Wombat instrument at the Open Pool Australian Lightwater reactor (OPAL) of the Australian Nuclear Science and Technology Organization (ANSTO) in Lucas Heights, Australia. Wombat is a high-intensity powder diffractometer allowing for fast data acquisition by using a two-dimensional position-sensitive detector. A wavelength of $\lambda = 0.2955$ nm was obtained by using a pyrolithic graphite monochromator. An oscillating radial collimator was placed in front of the detector in order to reduce background noise. The bar-type sample was placed vertically within the vanadium sample holder in the center of the instrument as shown in Figure 2. In the first run, the virgin sample was measured at the initial position with a rotational angle of $\chi = 0$. After poling, the sample was in an external setup for 30 s at room-temperature under 5 kV·mm^{-1}, the poled samples were measured again, collecting diffraction patterns for $\chi = (0;10;\ldots;180)°$. This procedure allows the analysis of potential textures.

D. Piezoresponse force microscopy

The PFM investigation has been accomplished using a commercial setup MFP-3D^{TM} (Asylum Research, Santa Barbara, CA, USA). The PFM method is based on the detection of local sample deformations induced by an electric *ac* field applied to a conductive PFM cantilever being in contact with the sample surface. Deflection of the cantilever is recorded as the vertical PFM (VPFM) signal. It provides information regarding the polarization component normal to the sample surface. The in-plane polarization component results in a torsional motion of the cantilever-tip, which is detected as the lateral PFM (LPFM) signal. PFM experiments were performed using p-doped silicon cantilevers (PPP-NCHR, Nanosensors, Neuchatel, Switzerland) with a force constant of 42 N·m^{-1} and a resonance frequency in the range of 204–497 kHz. For domain visualization, an *ac*

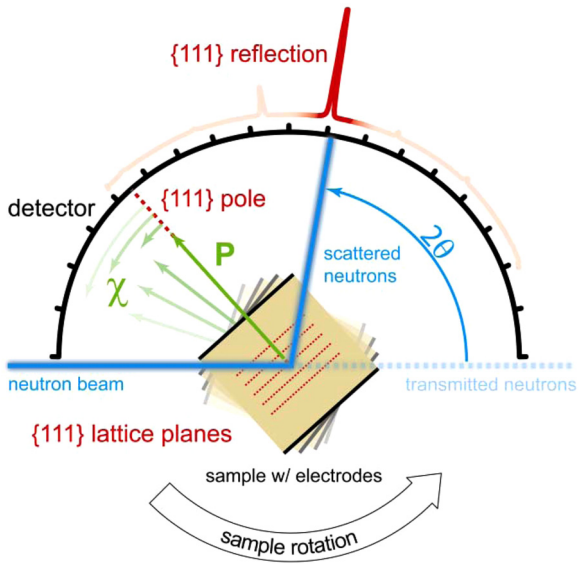

FIG. 2. Schematical top view of the constant wavelength, angle-dispersive neutron diffraction experiments at the Wombat instrument (ANSTO).

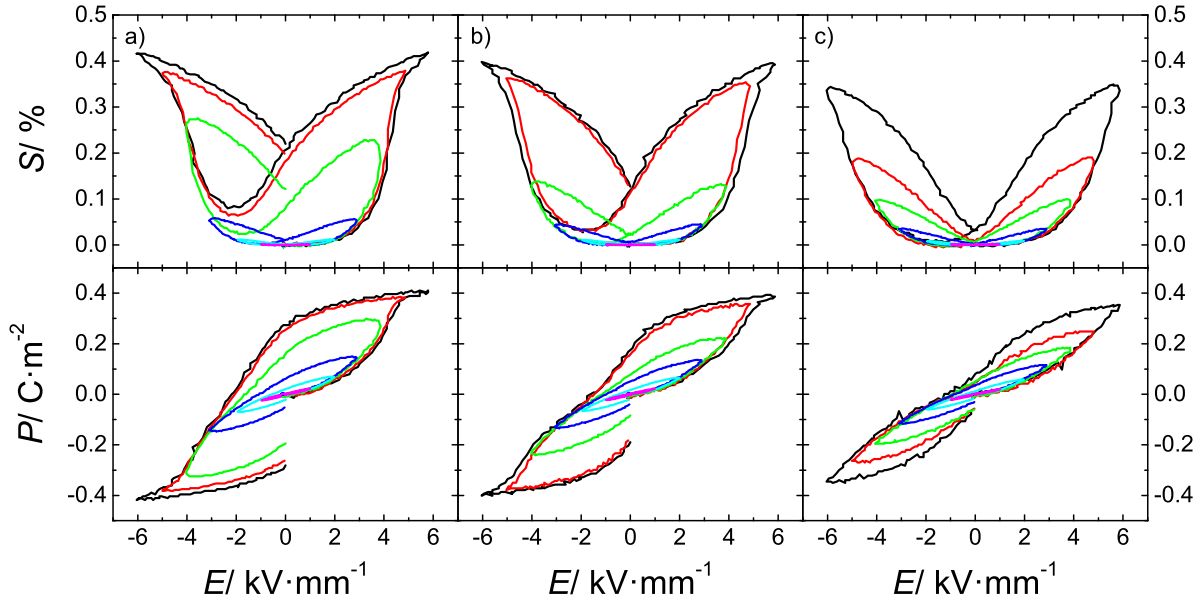

FIG. 3. Strain S and polarization P as a function of electric field for (a) 2BZT, (b) 3BZT, and (c) 4BZT with varying electric field amplitudes.

voltage with the amplitude $U_{ac} = 5$ V and frequency $f = 50$ kHz was applied to the tip. In order to study the polarization switching, an area of 5×5 μm^2 was locally poled by applying either positive or negative *dc* voltage, V_{dc}, up to 30 V. The acquired PFM data were analyzed by MatLab (The MathWorks, Inc., Natick, MA, USA) and WSxM software (Nanotec Electronica, Madrid, Spain).[30]

IV. RESULTS

A. Electrical properties

Figure 3 presents $P(E)$ and $S(E)$ loops for different maximum electric fields from 1 kV·mm^{-1} up to 6 kV·mm^{-1}. For 2BZT, cycling with a maximum electric field of 4 kV·mm^{-1} results in the development of the typical butterfly loop with significant S_{rem} and S_{neg}. For an amplitude of 5 kV·mm^{-1}, the polarization for 2BZT reaches saturation at $E_{sat} = 4.7$ kV·mm^{-1}, denoted by a bend in $P(E)$. Moreover, the strain in the first half-cycle rapidly increases up to 5 kV·mm^{-1} but the slope decreases notably close to the maximum field. The maximum slope $\Delta S/\Delta E$ is measured at about 4 kV·mm^{-1}.

The intermediate composition 3BZT depicts a transition between the other two materials. In comparison to 2BZT, higher fields are required for establishing a sizable S_{rem}; however, at the same time saturation occurs at a higher field $E_{sat} = 5.1$ kV·mm^{-1}. The usable unipolar strain found for 3BZT for $E \geq 5$ kV·mm^{-1} is larger than for 2BZT.

For 4BZT, no saturation in $P(E)$ is observed and the $S(E)$ hysteresis does not exhibit the typical butterfly shape but retains the "sprout" shape up to the highest employed electric field. Among all compositions, the usable strain for $E_{max} = 6$ kV·mm^{-1} is the highest for 4BZT.

It is noteworthy that at low fields ≤ 2 kV·mm^{-1} the S(E) loops and P(E) loops are remarkably similar among all compositions. The strain hysteresis exhibits only small remanent and negative strain, and the $P(E)$ loops are thin ellipses with accordingly small P_{rem}. This resemblance at low electric fields is also observed in the small-signal properties. In the unpoled state, the piezoelectric coefficient d_{33} is zero. Upon application of an electric field, d_{33} is increasing with similar field dependence for all compositions. For example, at 1 kV·mm^{-1} the discrepancy among the three compositions is as small as 1 pC·N^{-1} or 5% as shown in Figure 4(b). For $E > 2$ kV·mm^{-1}, the d_{33} for 2BZT notably deviates from the other two compositions. At a characteristic electric field $E_{sat} = 3.5$ kV·mm^{-1}, saturation is reached, indicated by a clear bend in the $d_{33}(E)$ curve. Upon removal of the electric field, a zero-field value of 141 pC·N^{-1} is obtained. For 3*BZT*, the field E_{sat} increases to 4 kV·mm^{-1} and the zero-field value decreases significantly to 87 pC·N^{-1}. For

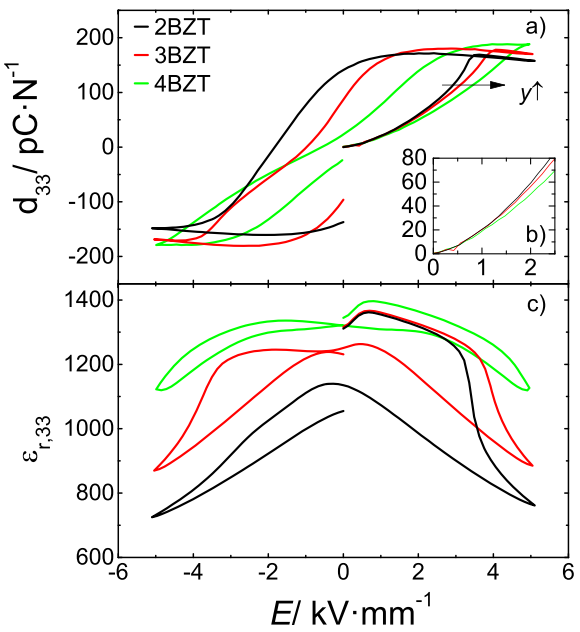

FIG. 4. Small-signal parameter piezoelectric constant d_{33} and relative permittivity $\varepsilon_{r,33}$ as a function of electric bias field.

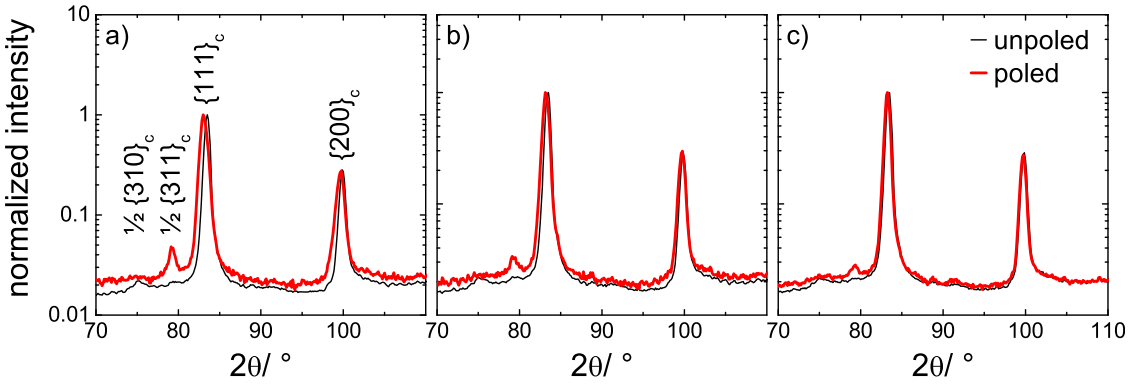

FIG. 5. Section of the neutron diffraction patterns for (a) 2BZT, (b) 3BZT, and (c) 4BZT depicting the $\{111\}_c$- and the $\{200\}_c$-type reflections along with the superlattice reflections before (unpoled) and after (poled) exposure to the electric field. Note the logarithmic scale for intensity, which is normalized to the peak intensity of the respective $\{111\}_c$ reflection.

4BZT, no saturation point is observed and d_{33} reaches a remanent value of 22 pC·N^{-1}. The value at maximum field, however, with 188 pC·N^{-1} is higher than for 2BZT (157 pC·N^{-1}) or 3BZT (170 pC·N^{-1}).

The relative permittivity $\varepsilon_{r,33}$ at zero-field is about 1300 with composition-dependent deviations being smaller than 2%. Similar to $d_{33}(E)$, the evolution of $\varepsilon_{r,33}$ with electric field is hard to discriminate among all compositions for $E < 2\,\mathrm{kV\cdot mm^{-1}}$. At higher fields, however, $\varepsilon_{r,33}$ drops significantly for 2BZT. Upon removal of the electric field, the zero-field permittivity of the poled state is notably diminished by about 20% compared to the unpoled state. For 3BZT, in contrast, the drop in $\varepsilon_{r,33}$ begins at higher electric fields with an inflection point at $E_{\mathrm{inflect}} = 3.9\,\mathrm{kV\cdot mm^{-1}}$ compared to $3.4\,\mathrm{kV\cdot mm^{-1}}$ for 2BZT. The zero-field permittivity is diminished by 6% with respect to the unpoled state. Finally, for 4BZT, the $\varepsilon_{r,33}(E)$ curve exhibits no abrupt drop, no inflection point, and only minute hysteretic behavior. Moreover, the effect of field exposure is reduced as the zero-field value decreases by merely 2%.

B. Neutron diffraction patterns

Figure 5 shows neutron diffraction patterns in the 2θ range from 70° to 110° encompassing both the $\{111\}_c$- and the $\{200\}_c$-type reflections before and after poling. In the initial state, the structure appears metrically cubic with symmetric and single Bragg peaks. The background is diffuse and satellite reflections are observed at $2\theta = \sim 75°$. These satellite peaks are very small in intensity, about 50 times weaker than the $\{111\}_c$ peak and only slightly higher than the background. Upon application of an electric field, the satellite peak at $2\theta = \sim 75°$ vanishes; however, a reflection of similar magnitude emerges at $2\theta = \sim 79°$. At the same time, the Bragg peaks exhibit a slight broadening. This broadening effect is strongest for $y = 0.02$ and decreases with increasing y. In addition, the shift of reflections towards lower angles denotes a change in lattice parameters, which is most pronounced for low BZT content. Based on the shift of the d_{200} lattice constant and the assumption that the structure is metrically cubic, the lattice constant can be said to decrease by approximately 0.6% for 2BZT, 0.3% for 3BZT, and 0.2% for 4BZT.

According to Figure 6, the application of an electric field establishes a rotation-angle dependence of peak intensity, that is, evolution of a crystallographic texture. The $\{111\}_c$ peak shows the largest broadening for $\chi = 0°$, i.e., when the q_{111} pole is parallel to the polarization vector and perpendicular to the lattice planes (cf. Figure 2). For $\chi = 90°$, the $\{111\}_c$ peak displays the smallest width and the highest intensity. This texture effect, however, decreases with increasing y. Consequently, no texture is discernible for 4BZT. Interestingly, the satellite reflection at $2\theta = \sim 79°$ likewise depicts an angular dependence in the 2BZT and 3BZT compositions, but not in 4BZT.

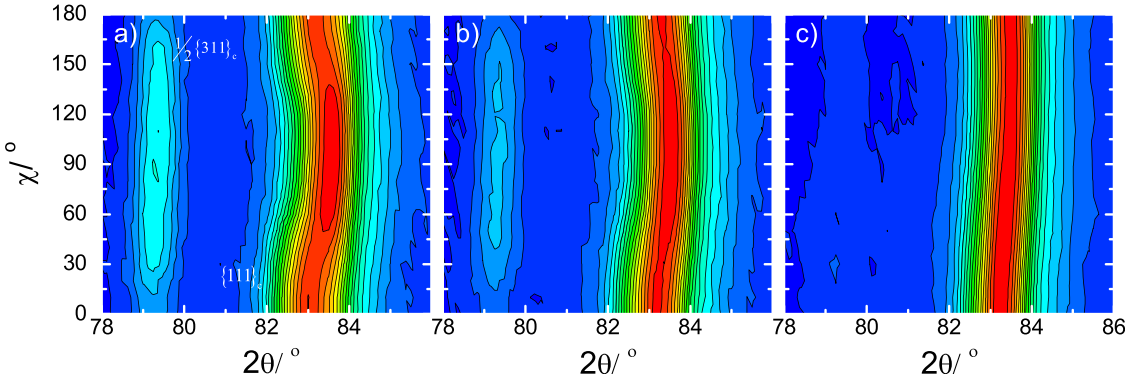

FIG. 6. Neutron diffraction patterns of the $^1/_2\{311\}_c$- and $\{111\}_c$-type reflections for poled (a) 2BZT, (b) 3BZT, and (c) 4BZT as a function of angle χ.

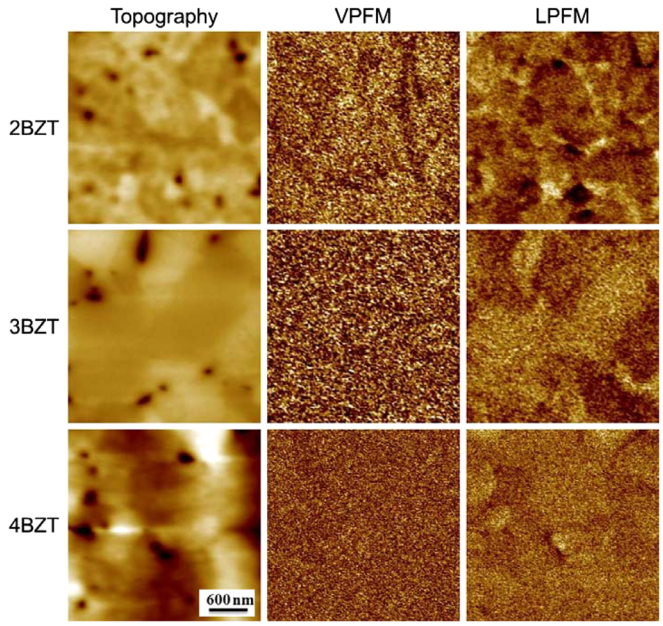

FIG. 7. PFM images of BNT-BKT-yBZT ceramics.

C. Piezoresponse force microscopy

It was demonstrated that the macroscopic large-signal constitutive behavior depends significantly on the applied maximum electric field. The PFM technique affords investigation of the interplay between the macroscopically determined properties and the polar structure measured at nanoscales.

Figure 7 provides PFM images taken from the samples with different BZT contents. For 2BZT, the VPFM signal is relatively weak, but regions with correlated piezoresponses can be distinguished. The LPFM image exhibits a better signal/noise ratio. For 3BZT, no piezoactive regions can be seen in the VPFM image, but the LPFM image still shows a certain contrast among grains with different crystallographic orientations. Finally, for 4BZT, both the VPFM and LPFM images show a negligible piezoresponse. Some contrast seen in the LPFM image is rather an artifact related to grain boundaries.

For 2BZT, application of *dc* bias voltage of ± 5 V resulted in the formation of macrodomains with the polarization directed along the applied field as displayed in Figure 8. The polarization inside the domains increases notably, as it is denoted by the stronger VPFM contrast, when the magnitude of the bias voltage increased from 5 V to 20 V and came to a saturation at higher voltage. For 3BZT, the VPFM signal inside the written domains increased rather gradually with the increasing bias voltage. It is significantly weaker at 5 V and a clear domain contour is not achieved below 15 V, while at larger voltage the intensity of the piezoresponse approaches values observed in 2BZT. Eventually, for 4BZT poling by ± 5 V did not result in the appearance of stable domain contrast, while at 15 V no clear contour but only an incomplete domain pattern was observed. At the same time, a pronounced asymmetry between VPFM signal in "positive" and "negative" domains was observed. At high voltage, the piezoresponse inside the negatively poled domains is approximately 100% larger than inside the positively poled domains. A similar asymmetry, albeit less pronounced, was also observed in 3BZT, while 2BZT shows a symmetric response relative to the polarity of applied bias.

The application of the *dc* bias has the same general effect on the LPFM[31] signal as for the VPFM signal; thus, it is not further shown and discussed.

V. DISCUSSION

2BZT at room temperature displays the behavior of a typical non-ergodic relaxor as, for example, a canonical PMN at low temperatures.[25–27] Hence, an electric field may

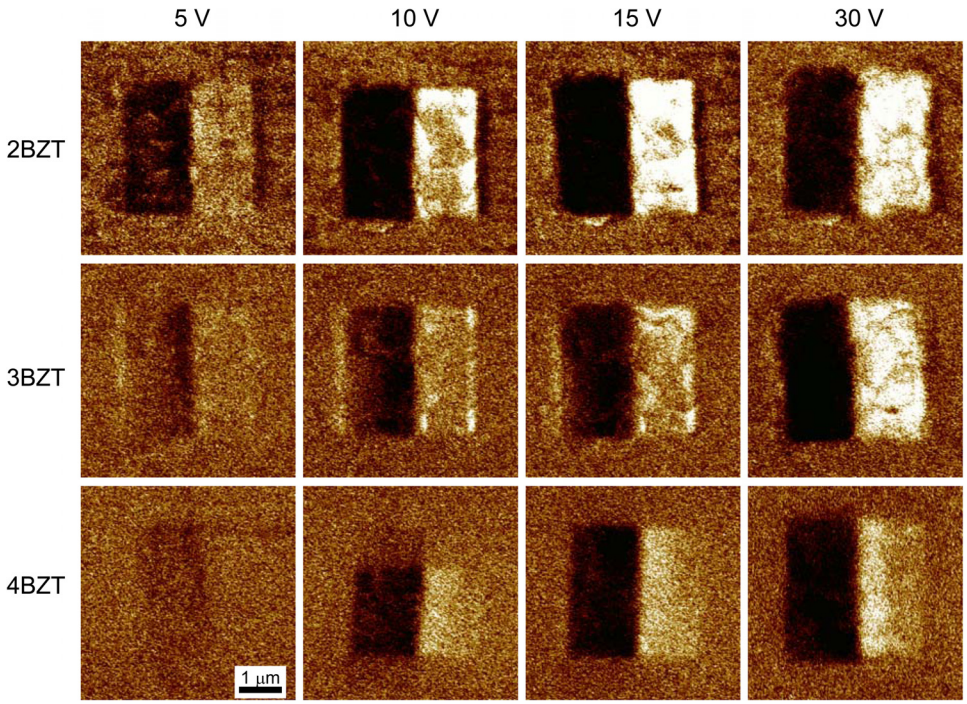

FIG. 8. VPFM after the internal square region was poled with different PFM tip bias voltages. The left and right sides of the square region were polarized by negative and positive bias fields, respectively.

induce a coalescence of PNRs into micro-domains. At small electric field amplitudes, the polarization increases slowly, which may partly be attributed to some PNRs merging. These domain nuclei, however, are mostly not stable and break up upon removal of the field as denoted by virtually zero remanent polarization. The observation of very similar $\varepsilon_{r,33}(E)$ and $d_{33}(E)$ curves among all three compositions for $E \leq 2\,\mathrm{kV\cdot mm^{-1}}$, furthermore, suggests that the polar volume fraction and the domain wall density are approximately similar. For 2BZT, a long-range order forms beyond a temperature- and time-dependent threshold electric field.[27,32]

The increased concentration of heterovalent Zn^{2+} ions enhances the quenched random fields and, consequently, decreases the *DoN*. As demonstrated previously,[25] the B-site ion Zn^{2+} affects the freezing process as represented by the depolarization temperature T_d dropping from 55 °C for 2BZT to below room temperature for 4BZT. Therefore, higher electric fields are required for inducing long-range order in 3BZT. The lower *DoN* can be discussed to be manifested in two different ways. First, the general correlation among all PNRs is decreased in equal measure. Second, frozen PNRs with strong correlation begin to coexist with dynamic, unfrozen PNRs. Different reports support the former possibility. By means of phase field simulations that also consider random fields introduced by point defects, a precursory state with frozen PNRs for $T > T_f$ was found.[33] This means that a partially non-ergodic state exists even before the majority of the PNRs collectively freezes. Using the spectroscopic PFM imaging method, Kalinin *et al.*[34] observed fast and slow relaxing regions in PMN-10PT. The former ones were interpreted as frozen spatial fluctuations of polarization, that is, a partially non-ergodic state. A PFM study by Shvartsman *et al.*[35] corroborates this finding with static nanodomains evidenced in both PMN and PMN-10PT beyond T_f. In addition, partially frozen domains were also discussed for the relaxor SBN as investigated by dielectric measurements[36] or second-harmonic generation.[37] For 3BZT, it may be, therefore, hypothesized that the amount of static domains decreases with respect to 2BZT. Consequently, the threshold electric field, which is necessary for inducing the transformation to ferroelectric state, increases from $4.7\,\mathrm{kV\cdot mm^{-1}}$ to $5.1\,\mathrm{kV\cdot mm^{-1}}$. Therefore, the strain is sprout-shaped up to a field amplitude E_{max} of $4\,\mathrm{kV\cdot mm^{-1}}$ with a small S_{rem} of 0.02%, which means that no stable long-range order is established throughout the sample.

Eventually, 4BZT is predominantly ergodic with dynamic and at most weakly correlated PNRs. The overall composition- and field-dependent trends are reflected in P_{rem} and S_{rem} as presented in Figure 9. The nearly zero S_{rem} for $E \leq 2\,\mathrm{kV\cdot mm^{-1}}$ found in all compositions demonstrates particularly well that the electromechanical properties below the threshold field are similar irrespective of the *DoN*. The effect of the dopant-induced decrease in *DoN* comes into effect predominantly at high electric fields as the incorporation of heterovalent Zn^{2+} ions causes a shift of the field-induced transition to higher field values.

Consequently, the electrical measurements suggest that the *DoN* indeed decreases with increasing BZT content. The question arises whether the structural evolution with electric

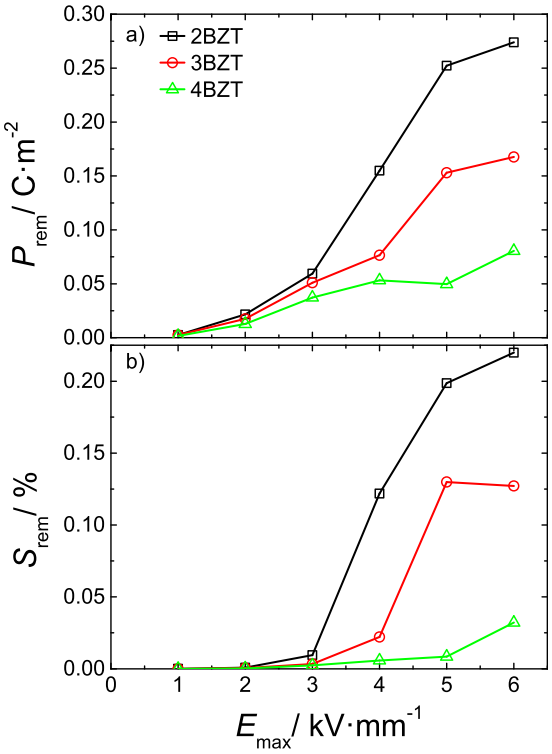

FIG. 9. Macroscopically measured (a) remanent polarization P_{rem} and (b) remanent strain S_{rem} as a function of electric field amplitude E_{max}.

field supports this view. In the initial state, all three compositions exhibit a close to cubic structure which is in agreement with reports on other canonical relaxors.[38,39] Due to the small size of the PNRs, any crystallographic distortions associated with the PNRs are of too small a coherence length to be detected by diffraction.

The neutron diffraction measurements, however, reveal weak satellite peaks at around 75° in the unpoled state. These reflections originate from tilting of the oxygen octahedra yielding a doubling of the unit cell and, thus, superlattice reflections emerge.[40] As described by Glazer, a superlattice reflection indicates a lower than cubic symmetry.[41] The here observed $^1/_2\{310\}_c$-type reflection(s) are caused by an in-phase oxygen octahedral tilting ($a^0a^0c^+$ in Glazer notation), which is consistent with the tetragonal *P*4*bm* structure. Therefore, it is concluded that all three materials, though metrically cubic, possess a tetragonal-like break in symmetry that allows for this type of tilting. This tilting system and tetragonal symmetry were also reported for the high-temperature phase of pure BNT.[40]

After poling, the $^1/_2\{310\}_c$ peak is largely diminished and another peak occurs near the $^1/_2\{311\}_c$-type reflection(s). This reflection is caused by antiphase oxygen octahedral tilting ($a^-a^-a^-$), which is consistent with tilting observed in rhombohedral *R*3*c* (Ref. 40) and *Cc* (Ref. 42) structures as reported for the room temperature phase of BNT. For that reason, it is concluded that the electric field triggers a phase transition from a metrically cubic phase with tetragonal superlattice peaks to a phase with rhombohedral-like superlattice peaks. Note, however, that the assignment of definite crystal structures for BNT-based materials based on satellite peaks is not unambiguous and often the cause of debate.

It is worthwhile noticing that the measured field-induced, irreversible increase of the unit cell volume is in line with macroscopic large-signal measurements published for the related lead-free system BNT-$BaTiO_3$-$K_{0.5}Na_{0.5}NbO_3$.[16] The reported remanent volume is on the same order of magnitude like the unit cell increase measured within this study.

The effect of the electric-field application on the structure strongly depends on the *DoN* as illustrated in Figure 10 for the $\{111\}_c$-type reflections. For the non-ergodic 2BZT, the reflection is broad where the broadening denotes likely peak splitting due to rhombohedral distortion. A sizable domain texture evolves with a preferential alignment of the polar axis (along the $\langle 111 \rangle$ direction) to the electric field, that is, close to 0° and 180°. In contrast, the ergodic 4BZT shows no measurable broadening or texture. This was expected from electrical measurements because of the small remanent polarization, small d_{33} at zero field, and virtually no change of permittivity upon field exposure. The intermediate composition 3BZT displays a transition between the predominantly non-ergodic 2BZT and the mainly ergodic 4BZT. Therefore, the structural measurements support the picture derived from electrical measurements, i.e., the *DoN* varies with BZT content and, consequently, the electrical and structural properties after electric-field exposure are altered to a great extent.

In order to validate this hypothesis, it is important to directly probe the microstructure at nanoscales by means of PFM to identify potentially frozen polar regions.

In the virgin state, 2BZT displays regions of correlated piezoresponse, even though they are not organized in mesoscale labyrinth structures, typical for lead-containing perovskite relaxors.[43] At the same time, 3BZT and 4BZT do not feature distinct domain patterns as confirmed by the autocorrelation function analysis illustrated in Figure 11. The autocorrelation function, $C(r_1,r_2)$, is obtained from original PFM images via the following transformation.

$$C(r_1, r_2) = \sum_{x,y} D(x, y)D(x + r_1, y + r_2). \quad (1)$$

$D(x,y)$ is the location dependent piezoresponse signal intensity. The shape of the autocorrelation function provides information about the symmetry and regularity of the polarization distribution. For 2BZT, a distinct central peak is found (autocorrelation images not shown) with the width

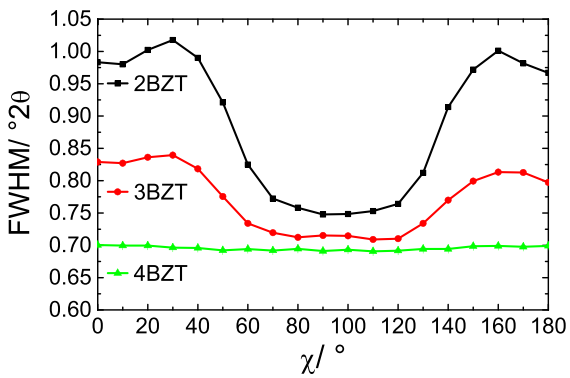

FIG. 10. Full width at half maximum (FWHM) of the $\{111\}_c$ peak as a function of rotation angle χ as determined by single peak fitting.

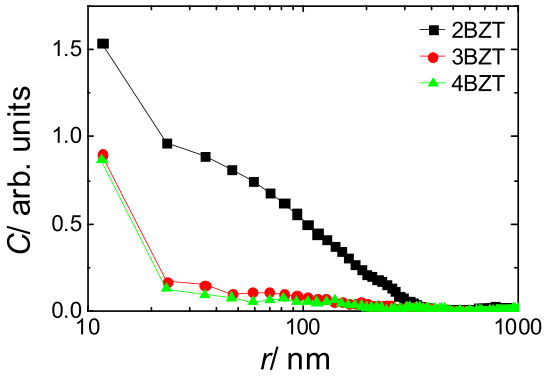

FIG. 11. Autocorrelation function of the VPFM averaged over all in-plane directions.

being a measure of the size of region of correlated piezoresponse, i.e., polarization.[44] At the same time, 3BZT and 4BZT show autocorrelation images typical for noise signal with a narrow peak related to the limited resolution and lock-in settings. This observation correlates with a crossover from a non-ergodic relaxor state with frozen PNRs in 2BZT to an ergodic-relaxor state with mainly dynamic PNRs in 4BZT. Featureless domain textures imply the potential existence of both static and dynamic PNRs that are not resolved by PFM. Therefore, the PFM measurements underpin the hypothesis of varying degrees of non-ergodicity with partly frozen PNRs.

As presented above, the local poling endorses formation of a long-range ferroelectric order in the compositions with both non-ergodic and ergodic relaxor behavior. The obtained PFM images confirm the ability for polarization switching manifested by the presence of inverse piezoresponse contrast of the regions poled by negative and positive field.

Macroscopic measurements demonstrate that P_{rem} and d_{33} increase with increasing electric field. The analogous tendency is observed at nanoscales. Figure 12 displays the voltage dependence of the piezoresponse averaged over the poled area. For all samples, the VPFM signal which is proportional to the longitudinal piezoelectric coefficient increased at moderate voltages and was saturated above a certain bias value V_{sat}. Similar to E_{sat} estimated from the macroscopic $P(E)$ measurements, V_{sat} increases with increasing BZT content. Therefore, the macroscopically observed

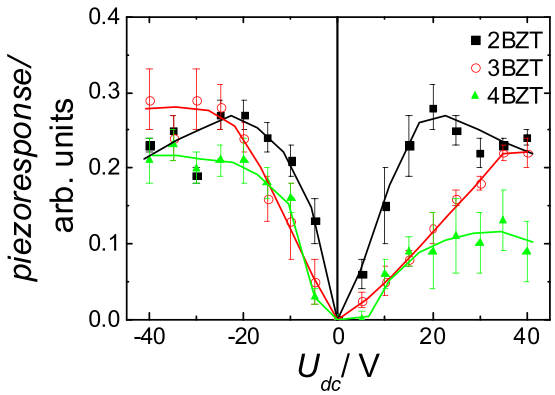

FIG. 12. Absolute values of the average piezoresponse inside the poled area as a function of poling voltage. Lines are drawn to guide the eye.

behavior is reflected by the submicroscopic behavior. The piezoelectric response of the 2BZT sample grew faster with voltage as compared to more ergodic 3BZT and ergodic 4BZT compositions (Fig. 12). In the last case, no stable domains were observed at voltages below 10 V. This observation is rationalized through a decrease in *DoN* causing an increase of the voltage required for overcoming the quenched random fields to establish long-range ferroelectric order.

It is conjectured that a lower *DoN* causes a decrease in the stability of the written domain, that is, the established long-range order. How important the consideration of time-dependent relaxation processes actually is, can be exemplified by the asymmetry of the piezoresponse in Figure 12. Keep in mind that the acquired PFM images correspond to a state at approximately 5–10 min after the bias field had been removed. That means that the piezoresponse signal can be strongly affected by relaxation of the induced state. Consequently, the observed asymmetry can be attributed to the different relaxation dynamics of the positively poled and negatively poled areas. Apparently, the negatively poled state is more stable which might be rationalized by the excess of negative charges at the surface, e.g., due to their higher mobility or due to effective n-type doping by chemical substitution. For the non-ergodic 2BZT, the relaxation plays a minor role and values of the remanent polarization and d_{33} coefficient are close to their saturation values. Consequently, the induced response is stable and rather symmetric. For the more ergodic compositions 3BZT and 4BZT, the field induced state is less stable. After the field is removed, the system starts to relax back to the state with random orientations of PNRs. However, in-depth investigations on the thermal and temporal stabilities remain reserved for future research.

VI. CONCLUSIONS

It was demonstrated that the concentration of heterovalent Zn^{2+} ions greatly affects the degree of non-ergodicity of the lead-free relaxor system $(1-y)$(0.81BNT-0.19BKT)-yBZT. The field-induced reflection broadening observed in neutron diffraction patterns decrease with increasing BZT content. This observation was rationalized with enhanced random fields, resulting in an increased amount of dynamic PNRs. Consequently, the field-induced transition into the long-range ordered state is impeded. As a result, the small- and large-signal constitutive behavior varies to a great extent at high electric fields. At low electric fields below $2\,kV{\cdot}mm^{-1}$, however, all compositions are virtually indistinguishable in terms of electric properties and crystal structure. It was, furthermore, found by PFM measurements that the relaxation mechanism depends on the polarity of the applied electrical field.

ACKNOWLEDGMENTS

This work was financially supported by the Deutsche Forschungsgemeinschaft (DFG) under SFB 595/A1. D. Gobeljic acknowledges the support of the European Commission within FP7 Marie Curie Initial Training Network "Nanomotion" (Grant Agreement No. 290158). Contributions by Jones were enabled through the U.S. National Science Foundation Award No. DMR-0746902. The Bragg Institute at ANSTO is acknowledged for provision of the neutron diffraction facilities through program Proposal No. 1366. The authors acknowledge fruitful discussions and technical assistance with the neutron measurements from several individuals including Andrew Studer, John Daniels, Hugh Simons, Shruti Banavara Seshadri, and Jennifer Forester.

[1]J. Macutkevic, J. Banys, and R. Grigalaitis, Appl. Phys. Lett. **98**, 016101 (2011).
[2]Off. J. Eur. Union **46**, 24 (2003).
[3]J. Rödel, W. Jo, K. T. P. Seifert, E. M. Anton, T. Granzow, and D. Damjanovic, J. Am. Ceram. Soc. **92**, 1153 (2009).
[4]B. Jaffe, R. S. Roth, and S. Marzullo, J. Appl. Phys. **25**, 809 (1954).
[5]K. T. P. Seifert, W. Jo, and J. Rödel, J. Am. Ceram. Soc. **93**, 1392 (2010).
[6]E. A. Patterson, D. P. Cann, J. Pokorny, and I. M. Reaney, J. Appl. Phys. **111**, 094105 (2012).
[7]A. Ullah, C. W. Ahn, A. Hussain, S. Y. Lee, H. J. Lee, and I. W. Kim, Curr. Appl. Phys. **10**, 1174 (2010).
[8]W. Jo, R. Dittmer, M. Acosta, J. Zang, C. Groh, E. Sapper, K. Wang, and J. Rödel, J. Electroceram. **29**, 71 (2012).
[9]R. Dittmer, E. Aulbach, W. Jo, K. G. Webber, and J. Rödel, Scr. Mater. **67**, 100 (2012).
[10]S. T. Zhang, A. B. Kounga, E. Aulbach, H. Ehrenberg, and J. Rödel, Appl. Phys. Lett. **91**, 112906 (2007).
[11]J. E. Daniels, W. Jo, J. Rödel, and J. L. Jones, Appl. Phys. Lett. **95**, 032904 (2009).
[12]H. Simons, J. Daniels, W. Jo, R. Dittmer, A. Studer, M. Avdeev, J. Rödel, and M. Hoffman, Appl. Phys. Lett. **98**, 082901 (2011).
[13]M. Hinterstein, M. Knapp, M. Hölzel, W. Jo, A. Cervellino, and H. Ehrenberg, J. Appl. Cryst. **43**, 1314 (2010).
[14]A. J. Royles, A. J. Bell, A. P. Jephcoat, A. K. Kleppe, S. J. Milne, and T. P. Comyn, Appl. Phys. Lett. **97**, 132909 (2010).
[15]R. Dittmer, W. Jo, J. Rödel, S. Kalinin, and N. Balke, Adv. Funct. Mater. **22**, 4208 (2012).
[16]W. Jo, T. Granzow, E. Aulbach, J. Rödel, and D. Damjanovic, J. Appl. Phys. **105**, 094102 (2009).
[17]K. Yoshii, Y. Hiruma, H. Nagata, and T. Takenaka, Jpn. J. Appl. Phys., Part 1 **45**, 4493 (2006).
[18]A. Sasaki, T. Chiba, Y. Mamiya, and E. Otsuki, Jpn. J. Appl. Phys., Part 1 **38**, 5564 (1999).
[19]I. Levin, I. M. Reaney, E. M. Anton, W. Jo, J. Rödel, J. Pokorny, L. A. Schmitt, H. J. Kleebe, M. Hinterstein, and J. L. Jones, Phys. Rev. B **87**, 024113 (2013).
[20]R. Dittmer, W. Jo, J. Daniels, S. Schaab, and J. Rödel, J. Am. Ceram. Soc. **94**, 4283 (2011).
[21]W. Kleemann, J. Mater. Sci. **41**, 129 (2006).
[22]L. Boltzmann, Wien. Ber. **96**, 891 (1887).
[23]K. Binder and A. P. Young, Rev. Mod. Phys. **58**, 801 (1986).
[24]D. Viehland, S. J. Jang, L. E. Cross, and M. Wuttig, J. Appl. Phys. **68**, 2916 (1990).
[25]D. Viehland, M. Wuttig, and L. E. Cross, Ferroelectrics **120**, 71 (1991).
[26]A. A. Bokov and Z. G. Ye, J. Mater. Sci. **41**, 31 (2006).
[27]Z. G. Ye, *Oxides* (Trans Tech Publications, Clausthal-Zellerfeld, 1998), Vol. 155-1, p. 81.
[28]R. Dittmer, W. Jo, E. Aulbach, T. Granzow, and J. Rödel, J. Appl. Phys. **112**, 014101 (2012).
[29]N. Balke, D. C. Lupascu, T. Granzow, and J. Rödel, J. Am. Ceram. Soc. **90**, 1081 (2007).
[30]I. Horcas, R. Fernandez, J. M. Gomez-Rodriguez, J. Colchero, J. Gomez-Herrero, and A. M. Baro, Rev. Sci. Instrum. **78**, 013705 (2007).
[31]See supplementary material at http://dx.doi.org/10.1063/1.4867157 for an exemplary figure.
[32]E. V. Colla, E. Y. Koroleva, N. M. Okuneva, and S. B. Vakhrushev, Phys. Rev. Lett. **74**, 1681 (1995).
[33]D. Wang, X. Ke, Y. Wang, J. Gao, Y. Wang, L. Zhang, S. Yang, and X. Ren, Phys. Rev. B **86**, 054120 (2012).

[34]S. V. Kalinin, B. J. Rodriguez, S. Jesse, A. N. Morozovska, A. A. Bokov, and Z. G. Ye, Appl. Phys. Lett. **95**, 142902 (2009).
[35]V. V. Shvartsman and A. L. Kholkin, J. Adv. Dielectr. **02**, 1241003 (2012).
[36]W. Kleemann, J. Dec, V. V. Shvartsman, Z. Kutnjak, and T. Braun, Phys. Rev. Lett. **97**, 065702 (2006).
[37]P. Lehnen, J. Dec, W. Kleemann, T. H. Woike, and R. Pankrath, Ferroelectrics **240**, 1547 (2000).
[38]P. Bonneau, P. Garnier, G. Calvarin, E. Husson, J. R. Gavarri, A. W. Hewat, and A. Morell, J. Solid State Chem. **91**, 350 (1991).
[39]A. H. Meitzler and H. M. O'Bryan, Jr., Proc. IEEE **61**, 959 (1973).
[40]G. O. Jones and P. A. Thomas, Acta Crystallogr., Sect. B **58**, 168 (2002).
[41]A. Glazer, Acta Crystallogr., Sect. B **28**, 3384 (1972).
[42]E. Aksel, J. S. Forrester, J. L. Jones, P. A. Thomas, K. Page, and M. R. Suchomel, Appl. Phys. Lett. **98**, 152901 (2011).
[43]V. V. Shvartsman, A. L. Kholkin, A. Orlova, D. Kiselev, A. A. Bogomolov, and A. Sternberg, Appl. Phys. Lett. **86**, 202907 (2005).
[44]V. V. Shvartsman and A. L. Kholkin, J. Appl. Phys. **101**, 064108 (2007).